

On-chip low-loss all-optical MoSe₂ modulator

MOHAMMED ALALOUL^{1,*}, JACOB B. KHURGIN², IBRAHIM AL-ANI¹, KHALIL AS'HAM¹, LUJUN HUANG³, HAROLDO T. HATTORI¹, AND ANDREY E. MIROSHNICHENKO^{1,*}

¹School of Engineering and Information Technology, University of New South Wales, Canberra, ACT 2612, Australia

²Electrical and Computer Engineering Department, Johns Hopkins University, Baltimore, MD 21218, USA

³School of Physics and Electronic Science, East China Normal University, Shanghai 200241, China

*Corresponding authors: m.alaloul@unsw.edu.au; andrey.miroshnichenko@unsw.edu.au

Compiled July 6, 2022

Monolayer transition metal dichalcogenides (TMDCs), like MoS₂, MoSe₂, WS₂, and WSe₂, feature direct bandgaps, strong spin-orbit coupling, and exciton-polariton interactions at the atomic scale, which could be harnessed for efficient light emission, valleytronics, and polaritonic lasing, respectively. Nevertheless, to build next-generation photonic devices that make use of these features, it is first essential to model the all-optical control mechanisms in TMDCs. Herein, a simple model is proposed to quantify the performance of a 35 μm long Si₃N₄ waveguide-integrated all-optical MoSe₂ modulator. Using this model, a switching energy of 14.6 pJ is obtained for a transverse-magnetic (TM) and transverse-electric (TE) polarised pump signals at $\lambda = 480$ nm. Moreover, maximal extinction ratios of 20.6 dB and 20.1 dB are achieved for a TM and TE polarised probe signal at $\lambda = 500$ nm, respectively, with an ultra-low insertion loss of < 0.3 dB. Moreover, the device operates with an ultrafast recovery time of 50 ps, while maintaining a high extinction ratio for practical applications. These findings facilitate modeling and designing novel TMDC-based photonic devices. © 2022

Optica Publishing Group

<http://dx.doi.org/10.1364/ao.XX.XXXXXX>

Two-dimensional (2D) materials have recently emerged as practical active materials for on-chip photonics [1–3]. Unlike bulk materials, these materials are easily integrated into underlying substrates by van der Waals (vdW) forces, which facilitate device fabrication by complementary metal-oxide semiconductor (CMOS) processes [4]. Moreover, these materials exhibit unique optoelectronic properties that are of interest from a scientific and technological perspective. In particular, monolayer transition metal dichalcogenides (TMDCs) have direct bandgaps, strong spin-orbit coupling, and exciton-polariton interactions at the atomic scale, which could be utilized for efficient light emission, valleytronics, and polaritonic lasing, respectively [5–8]. To design and build functional devices that make use of these features, it is first essential to model the electrical and all-optical control mechanisms in TMDCs. So far, there has not been a comprehensive model that describes these mechanisms in TMDC

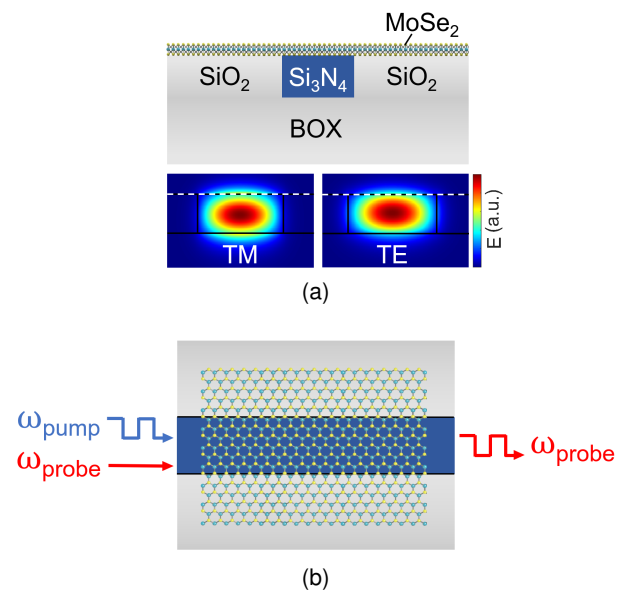


Fig. 1. (a) Cross-sectional view of the on-chip modulator. Bottom panel: electric field profile (E) of the TM and TE modes at $\lambda = 450$ nm. The white dashed line represents the MoSe₂ plane. (b) Top view. The pump signal modulates a probe signal. MoSe₂: molybdenum diselenide, Si₃N₄: silicon nitride, SiO₂: silicon dioxide, BOX: buried oxide.

monolayers. To fill this gap, we model the saturable absorption and all-optical modulation mechanisms in monolayer molybdenum diselenide (MoSe₂), which is integrated into silicon nitride (Si₃N₄) waveguides. To the best of our knowledge, a waveguide-integrated all-optical MoSe₂ modulator has not been reported in the literature. This model can also describe these mechanisms in other TMDCs and 2D semiconductors.

The device structure is presented in Fig. 1. A 750×250 nm Si₃N₄ wire waveguide on top of a $10 \mu\text{m}$ thick buried oxide (BOX) layer guides the incoming light to the modulator section, where the MoSe₂ monolayer is located. The waveguide dimensions are optimized to achieve an ultra-low propagation loss. Si₃N₄ waveguides with similar dimensions have been demonstrated in [9], where the optical mode is guided with

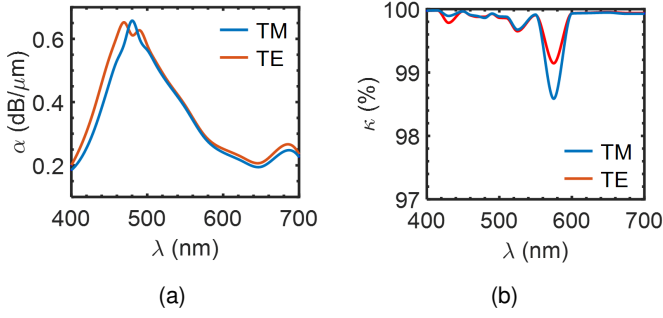


Fig. 2. (a) Absorption coefficients (α) and coupling efficiencies (κ) of the TM and TE modes as a function of wavelength (λ).

a propagation loss of merely 1.7 dB/cm. The waveguide supports the transverse-magnetic (TM) and transverse-electric (TE) modes. The computed absorption coefficient (α) of each mode is presented in Fig. 2a, which is attributed to the MoSe₂ monolayer because it is the only absorbing material within the structure. Highly efficient coupling ($> 98\%$) between the Si₃N₄ waveguide and the modulator section is obtained for both modes, as shown in Fig. 2b. Simulations were conducted in Lumerical MODE with a 0.7 nm thick MoSe₂ monolayer. The refractive index data of monolayer MoSe₂ are taken from [10]. Perfect matching layer (PML) boundary conditions were used in the simulations. Similar results are obtained using metal boundary conditions.

The modulation relies on the exciton bleaching mechanism [11]. As depicted in Fig. 3a, the MoSe₂ monolayer absorbs an incident pump signal photon, which generates an interband exciton at visible wavelengths. When a sufficiently intense pump signal is applied, exciton bleaching occurs because of electron-hole plasma screening or band filling [12]. Due to the reduced dimensionality in 2D materials, screening is reduced. Then, exciton bleaching is most likely due to band filling [11]. Taking that into account, when the generated excitons fill the conduction and valence band states, a probe signal photon with an energy $\hbar\omega_{\text{probe}} \leq \hbar\omega_{\text{pump}}$ is transmitted, as shown in Fig. 3b. By taking advantage of this phenomenon, amplitude modulation is realized [13], where the probe signal is HIGH when the pump signal is ON, whereas it is LOW when the pump signal is OFF, as shown in Fig. 3c. Herein, the band structure of monolayer MoSe₂ is described by the dispersion relations of the conduction (E_c) and valence (E_v) bands:

$$E_c(k) = \frac{E_g}{2} + \frac{\hbar^2 k^2}{2m_c} \quad (1)$$

$$E_v(k) = -\frac{E_g}{2} - \frac{\hbar^2 k^2}{2m_v} \quad (2)$$

where $E_g = 1.55$ eV is the energy bandgap [14], $m_c = 0.545$ and $m_v = 0.647$ are the effective masses of electrons and holes in monolayer MoSe₂ [15], respectively, and $k = \sqrt{2\pi n}$ is the wavevector, with n being the carrier density. For a pump signal photon with an energy $\hbar\omega_{\text{pump}}$, transitions are blocked when the photogenerated excitons fully occupy the states. From Fig. 3, this occurs when:

$$\hbar\omega_{\text{pump}} = E_c(k) - E_v(k) = E_g + \frac{\hbar^2 k^2}{2m_r} \quad (3)$$

where $m_r = (1/m_c + 1/m_v)^{-1}$ is the reduced effective mass. The corresponding photogenerated exciton density is given by:

$$n = \frac{m_r}{\pi\hbar^2} (\hbar\omega_{\text{pump}} - E_g) \quad (4)$$

Then, the switching energy of the modulator (U_{sw}) is calculated by multiplying the total number of photogenerated excitons (m) by $\hbar\omega_{\text{pump}}$ [16]:

$$U_{\text{sw}} = \sum_m \hbar\omega_{\text{pump}} \quad (5)$$

where $m = nWL_{\text{mod}}$ is the total number of photogenerated excitons, W is the waveguide width, and L_{mod} is the modulator length. For $L_{\text{mod}} = 35 \mu\text{m}$, $\sim 99\%$ of the pump signal is absorbed for both the TM and TE polarisations, where the absorbed power fraction (A) is calculated using the Beer-Lambert Law $A(L_{\text{mod}}) = 1 - 10^{-(\alpha/10)*L_{\text{mod}}}$. A fraction of the absorbed light power is non-saturable (A_{ns}), and does not contribute to the modulation mechanism. Besides, there is a small coupling loss, $\Gamma = 1 - \kappa$, between the Si₃N₄ waveguide and the modulator section. To account for these losses, the effective switching energy (U_{eff}) is calculated as [13]:

$$U_{\text{eff}} = \frac{U_{\text{sw}}(1 + \Gamma + A_{\text{WG}})}{A * (1 - A_{\text{ns}})} \quad (6)$$

where $A_{\text{ns}} = (1.08/25.58) * 100\% = 4.22\%$ is taken based on the values reported for a MoSe₂ monolayer in [17]. $A_{\text{WG}} = 1 - 10^{-(\alpha_{\text{WG}}/10)*L_{\text{mod}}}$ is the Si₃N₄ waveguide loss that is not related to MoSe₂, where $\alpha_{\text{WG}} = 1.7$ dB/cm. In Fig. 2a), the absorption peak of the waveguide-integrated MoSe₂ occurs at ~ 480 nm, which is chosen as the pump signal wavelength. The resulting U_{eff} is ~ 14.6 pJ for both the TE- and TM-polarised modes, where the absorption coefficients of both modes at that wavelength are almost similar.

The modulation efficiency is quantified by the extinction ratio (ER), where $ER = 10\log_{10}(T_{\text{on}}/T_{\text{off}})$ [13]. T_{on} and T_{off} represent the transmittance of the probe signal when the pump signal is switched ON and OFF, respectively. Here, we consider operation where a pump signal with an energy $U \geq U_{\text{eff}}$ is applied. Then, T_{on} and T_{off} are given by [18]:

$$T_{\text{on}} = [1 - (\Gamma + A * A_{\text{ns}})] * (1 - \Gamma) \quad (7)$$

$$T_{\text{off}} = [1 - (\Gamma + A)] * (1 - \Gamma) \quad (8)$$

where A is the absorbance calculated using the Beer-Lambert law. In addition, the insertion loss (IL) of the device is calculated as $IL = 10\log(1/T_{\text{on}})$. The resulting ER and IL of the device are presented in Fig. 4 for a broadband wavelength region. First, it is found that the IL is as low as < 0.3 dB across the studied band, which is attributed to the ultra-low coupling loss of the modulator. A remarkable ER ratio of 20.6 dB and 20.1 dB are achievable for a 500 nm probe signal with the TM and TE polarisations, respectively. Moreover, the ER plot follows the trend of the absorption coefficient plot that was presented in Fig. 2a. A higher absorption of the probe signal results in a greater extinction ratio between T_{on} and T_{off} . Additionally, highly efficient modulation is attainable at other wavelengths, where the lowest ER is 7.1 dB and 6.7 dB for the TM and TE polarised modes, respectively, at $\lambda_{\text{probe}} = 650$ nm.

The modulation performance of the device is characterized by its recovery time, which is fundamentally limited by the cooling mechanisms in the MoSe₂ monolayer. Following photoexcitation

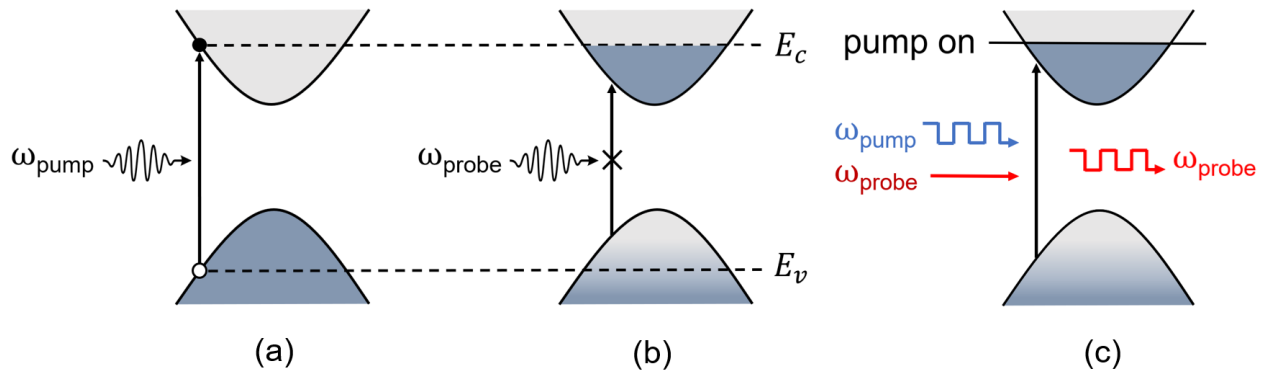


Fig. 3. (a) Interband absorption of a pump photon with an energy $\hbar\omega_{\text{pump}}$. (b) Probe photon transmitted after applying a pump signal with sufficiently high intensity. (c) Transmission of the probe signal, as determined by the pump signal amplitude. Black and white circles represent electrons and holes, respectively. Darker shades represent filled energy states.

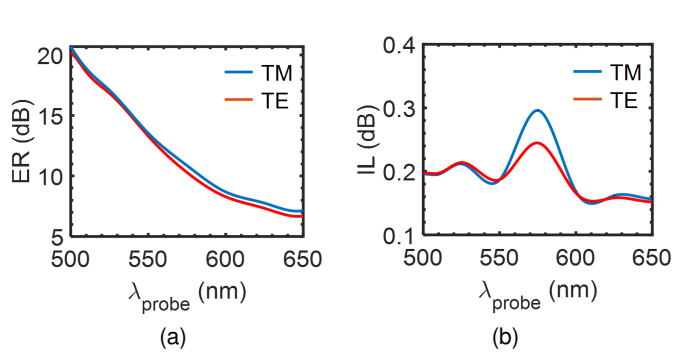


Fig. 4. (a) Extinction ratio (ER) and (b) insertion loss (IL) as a function of the probe signal wavelength (λ_{probe}) for the TM and TE modes.

by a pump signal, exciton-exciton annihilation occurs within a few tens of picoseconds, while full electron-hole recombination can last for hundreds of picoseconds [19]. The cooling dynamics in monolayer MoSe₂ can be modelled as [19]:

$$N(t) = \frac{N_0}{1 + \gamma N_0 t} \quad (9)$$

where $N(t)$ is the exciton density as a function of time, N_0 is the initial exciton density, and $\gamma = 0.4 \text{ cm}^2/\text{s}$ is the exciton-exciton annihilation rate [19]. At $\lambda_{\text{pump}} = 480 \text{ nm}$, the photogenerated exciton density is $1.28 \times 10^{14} \text{ cm}^{-2}$. Using these parameters, Eq. 9 is plotted in the time range of 5 – 175 ps in Fig. 5, which is similar to the one presented in [19]. It is observed that recovery mostly occurs within tens of picoseconds by the exciton-exciton annihilation process. As previously explained, photogenerated excitons fill the states, leading to exciton bleaching and transmission of the probe signal. Therefore, the transmission of the probe signal follows the trend of the plotted curve in Fig. 5. Even though full recombination occurs in hundreds of picoseconds, for practical switching applications, it would be sufficient to operate the modulator with a time interval of 50 ps following a pump excitation, where the corresponding $N(t)/N_{\text{max}} = 10\%$. In compensation for faster operation, the ER decreases because of the reduced contrast between the ON and OFF states. For instance, for a negligible coupling and non-saturable losses, $ER = 20 \text{ dB}$, where $T_{\text{on}} = 100\%$, and $T_{\text{off}} = 1\%$. However, while

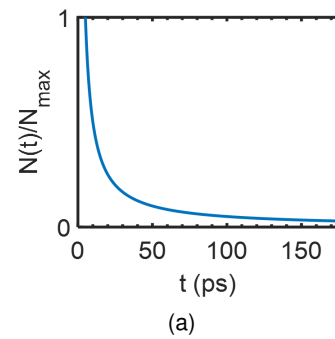


Fig. 5. Normalized exciton density as a function of time.

operating at a 50 ps time interval, $T_{\text{on}} = 100\%$, and $T_{\text{off}} = 10\%$, resulting in a 10 dB extinction ratio, which is highly desirable for practical applications. The ultrafast response of this device could be harnessed for building saturable absorbers, pulsed lasers, and for visible light switches. Moreover, the proposed model can describe the saturable absorption and all-optical modulation mechanisms in other TMDCs and 2D semiconductors by tuning the modelling parameters, e.g., material absorption, bandgap, effective masses, and exciton-exciton annihilation rate.

Funding. Australian Research Council (DP200101353).

Acknowledgments. This work was supported by the Australian Research Council (DP200101353).

Disclosures. The authors declare no conflicts of interest.

Data Availability Statement. The authors confirm that the data supporting the findings of this study are available within the article.

REFERENCES

1. Z. Sun, A. Martinez, and F. Wang, Nat. Photonics **10**, 227 (2016).
2. D. Akinwande, C. Huyghebaert, C.-H. Wang, M. I. Serna, S. Goossens, L.-J. Li, H.-S. P. Wong, and F. H. Koppens, Nature **573**, 507 (2019).
3. M. Alaloul and J. B. Khurgin, IEEE Photonics J. **13**, 1 (2021).
4. M. Alaloul and M. Rasras, JOSA B **38**, 602 (2021).
5. L. Huang, A. Krasnok, A. Alu, Y. Yu, D. Neshev, and A. Miroshnichenko, Reports on Prog. Phys. **85**, 046401 (2021).
6. A. Rauschenbeutel and P. Schneeweiss, Nat. Photonics **16**, 261 (2022).
7. A. Kavokin, T. C. Liew, C. Schneider, P. G. Lagoudakis, S. Klembt, and S. Hoefling, Nat. Rev. Phys. pp. 1–17 (2022).

8. H. Ou, H. Matsuoka, J. Tempia, T. Yamada, T. Takahashi, K. Oi, Y. Takaguchi, T. Endo, Y. Miyata, C.-H. Chen *et al.*, *ACS nano* **15**, 12911 (2021).
9. A. Buchberger, J. Pulko, D. Morecroft, O. Basso, J. Kraft, and A. Bergmann, "Modelling propagation loss of pecvd silicon nitride strip waveguides: Evaluation and assessment of width dependency," in *2021 Conference on Lasers and Electro-Optics (CLEO)*, (IEEE, 2021), pp. 1–2.
10. C. Hsu, R. Frisenda, R. Schmidt, A. Arora, S. M. De Vasconcellos, R. Bratschitsch, H. S. van der Zant, and A. Castellanos-Gomez, *Adv. optical materials* **7**, 1900239 (2019).
11. R. Amin, J. B. Khurgin, and V. J. Sorger, *Opt. express* **26**, 15445 (2018).
12. D. S. Chemla and D. A. Miller, *JOSA B* **2**, 1155 (1985).
13. M. Alaloul and J. B. Khurgin, *IEEE J. Sel. Top. Quantum Electron.* **28**, 1 (2022).
14. S. Tongay, J. Zhou, C. Ataca, K. Lo, T. S. Matthews, J. Li, J. C. Grossman, and J. Wu, *Nano letters* **12**, 5576 (2012).
15. A. Rawat, N. Jena, A. De Sarkar *et al.*, *J. Mater. Chem. A* **6**, 8693 (2018).
16. M. Alaloul and M. Rasras, *ACS omega* **6**, 7576 (2021).
17. X. Tian, R. Wei, Z. Ma, and J. Qiu, *ACS Appl. Mater. & Interfaces* **14**, 8274 (2022).
18. M. Alaloul and J. B. Khurgin, *Opt. Express* **30**, 1950 (2022).
19. B. Liu, Y. Meng, X. Ruan, F. Wang, W. Liu, F. Song, X. Wang, J. Wu, L. He, R. Zhang *et al.*, *Nanoscale* **9**, 18546 (2017).

FULL REFERENCES

1. Z. Sun, A. Martinez, and F. Wang, "Optical modulators with 2d layered materials," *Nat. Photonics* **10**, 227–238 (2016).
2. D. Akinwande, C. Huyghebaert, C.-H. Wang, M. I. Serna, S. Goossens, L.-J. Li, H.-S. P. Wong, and F. H. Koppens, "Graphene and two-dimensional materials for silicon technology," *Nature* **573**, 507–518 (2019).
3. M. Alaloul and J. B. Khurgin, "Plasmonic photovoltaic double-graphene detector integrated into tin slot waveguides," *IEEE Photonics J.* **13**, 1–8 (2021).
4. M. Alaloul and M. Rasras, "Plasmon-enhanced graphene photodetector with cmos-compatible titanium nitride," *JOSA B* **38**, 602–610 (2021).
5. L. Huang, A. Krasnok, A. Alu, Y. Yu, D. Neshev, and A. Miroshnichenko, "Enhanced light-matter interaction in two-dimensional transition metal dichalcogenides," *Reports on Prog. Phys.* **85**, 046401 (2021).
6. A. Rauschenbeutel and P. Schneeweiss, "Chiral quantum optics goes electric," *Nat. Photonics* **16**, 261–262 (2022).
7. A. Kavokin, T. C. Liew, C. Schneider, P. G. Lagoudakis, S. Klembt, and S. Hoeffling, "Polariton condensates for classical and quantum computing," *Nat. Rev. Phys.* pp. 1–17 (2022).
8. H. Ou, H. Matsuoka, J. Tempia, T. Yamada, T. Takahashi, K. Oi, Y. Takaguchi, T. Endo, Y. Miyata, C.-H. Chen *et al.*, "Spatial control of dynamic p–i–n junctions in transition metal dichalcogenide light-emitting devices," *ACS nano* **15**, 12911–12921 (2021).
9. A. Buchberger, J. Pulko, D. Morecroft, O. Basso, J. Kraft, and A. Bergmann, "Modelling propagation loss of pecvd silicon nitride strip waveguides: Evaluation and assessment of width dependency," in *2021 Conference on Lasers and Electro-Optics (CLEO)*, (IEEE, 2021), pp. 1–2.
10. C. Hsu, R. Frisenda, R. Schmidt, A. Arora, S. M. De Vasconcelos, R. Bratschitsch, H. S. van der Zant, and A. Castellanos-Gomez, "Thickness-dependent refractive index of 1l, 2l, and 3l mos₂, mose₂, ws₂, and wse₂," *Adv. optical materials* **7**, 1900239 (2019).
11. R. Amin, J. B. Khurgin, and V. J. Sorger, "Waveguide-based electro-absorption modulator performance: comparative analysis," *Opt. express* **26**, 15445–15470 (2018).
12. D. S. Chemla and D. A. Miller, "Room-temperature excitonic nonlinear-optical effects in semiconductor quantum-well structures," *JOSA B* **2**, 1155–1173 (1985).
13. M. Alaloul and J. B. Khurgin, "High-performance all-optical modulator based on graphene-hbn heterostructures," *IEEE J. Sel. Top. Quantum Electron.* **28**, 1–8 (2022).
14. S. Tongay, J. Zhou, C. Ataca, K. Lo, T. S. Matthews, J. Li, J. C. Grossman, and J. Wu, "Thermally driven crossover from indirect toward direct bandgap in 2d semiconductors: Mose₂ versus mos₂," *Nano letters* **12**, 5576–5580 (2012).
15. A. Rawat, N. Jena, A. De Sarkar *et al.*, "A comprehensive study on carrier mobility and artificial photosynthetic properties in group vi b transition metal dichalcogenide monolayers," *J. Mater. Chem. A* **6**, 8693–8704 (2018).
16. M. Alaloul and M. Rasras, "Low insertion loss plasmon-enhanced graphene all-optical modulator," *ACS omega* **6**, 7576–7584 (2021).
17. X. Tian, R. Wei, Z. Ma, and J. Qiu, "Broadband nonlinear optical absorption induced by bandgap renormalization in cvd-grown monolayer mose₂," *ACS Appl. Mater. & Interfaces* **14**, 8274–8281 (2022).
18. M. Alaloul and J. B. Khurgin, "Electrical control of all-optical graphene switches," *Opt. Express* **30**, 1950–1966 (2022).
19. B. Liu, Y. Meng, X. Ruan, F. Wang, W. Liu, F. Song, X. Wang, J. Wu, L. He, R. Zhang *et al.*, "Coupled relaxation channels of excitons in monolayer mose₂," *Nanoscale* **9**, 18546–18551 (2017).